n-Beam Lattice Images.
I. Experimental and Computed Images from $W_4Nb_{26}O_{77}$

BY J. G. ALLPRESS

Division of Tribophysics, CSIRO, University of Melbourne, Parkville 3052, Australia

ELIZABETH A. HEWAT

Physics Department, University of Melbourne, Parkville 3052, Australia,

A. F. MOODIE

Division of Chemical Physics, CSIRO, P. O. Box 160, Clayton, Victoria 3168, Australia

AND J. V. SANDERS

Division of Tribophysics, CSIRO, University of Melbourne, Parkville 3052, Australia

A series of through-focus lattice images has been obtained with an electron microscope for single crystals of $W_4Nb_{26}O_{77}$ set at an orientation to give mainly a systematic set of 00*l* reflexions. Dynamical *n*-beam computations ($n=435$) have been made for a crystal in this orientation to determine the values of the amplitudes and phases of the diffracted beams. Subsequently, the fringe profiles for lattice images have been computed for various thicknesses of crystal and defects of focus. When the experimental factors, including instrument aberrations, are taken into account, good agreement between computed and observed fringes is obtained. An earlier assumption of direct correlation of features in under-focused images with structure in the crystal, is found to be valid, at least for this compound.

Introduction

Modern electron microscopes have sufficient resolution to produce images of periodic and nonperiodic structural features on a scale comparable with atomic dimensions. Lattice images of crystals are now widely used as a means of testing the resolution of these instruments and calibrating their magnification; fringe spacings down to 0·088 nm have been recorded (Yada & Hibi, 1969). These images, which are usually obtained by allowing only one or two diffracted beams to pass through the objective aperture together with the transmitted beam (Dowell, 1963), contain simple interference fringes. However, images to which many diffracted beams contribute should contain much more information (Miyake, Fujiwara, Tokonami & Fujimoto, 1964) and it is important to understand the relationship between the crystal structure and the appearance of the fringes in order to interpret correctly lattice images of this sort.

This paper presents the results of an experimental and theoretical study of lattice images from the complex oxide $W_4Nb_{26}O_{77}$. The study was limited to the relatively simple case of images formed by contributions from a restricted number of 00*l* ($|l| \le 5$) reflexions from a thin crystal of $W_4Nb_{26}O_{77}$ oriented so that the systematic set of 00*l* reflexions dominated the electron diffraction pattern. The reasons for selecting such an apparently unusual material were as follows:

(*a*) The compound has a large unit cell ($c \sim 2\cdot6$ nm), and therefore lattice images were readily obtained using the relatively poor resolution (*ca.* 0·5 nm) available to us.

(*b*) Previous electron microscope studies of $W_4Nb_{26}O_{77}$ (Allpress, Sanders & Wadsley, 1969) had shown that the lattice images contained distinctive contrast. A simple interpretation of this contrast was made in terms of the crystal structure.

(*c*) The crystals contain planar faults, which provide convenient reference markers.

(*d*) The material is stable in the electron beam of the microscope.

(*e*) The material is brittle, and very thin fragments can be prepared simply by grinding, without introducing additional defects.

The experimental program involved the recording of through-focus series of images on either side of the Gaussian image plane. The calculations, which were based on the X-ray determination of the structure of a single crystal of $W_4Nb_{26}O_{77}$ (Andersson, Mumme, & Wadsley, 1966), involved determining the dynamical amplitudes and phases of diffracted beams of electrons for a series of different crystal thickness, and using these to compute images at specific deviations from the Gaussian image plane. Instrumental effects of lens aberrations, beam divergence, and depth-of-focus, were considered separately.

The contrast in the lattice images is produced by the interaction of a number of diffracted beams (ten in our case), and the appearance of the fringes therefore depends on the amplitudes and phases of these beams. There is ample evidence that except for the very thinnest

crystals, the kinematic theory gives quite incorrect values for the intensities and phases of diffracted beams of electrons (Cowley, 1967). Therefore, it seemed necessary from the outset to use dynamical computations to establish the amplitudes and phases of the diffracted beams, and their variation with crystal thickness. In this paper, the results of an accurate dynamical calculation are used for comparison with experiment to establish the validity of the computation. A subsequent paper (Lynch & O'Keefe, 1972) will compare this calculation with more rapid approximate computations, and also with results from kinematic theory.

2. Theory

2.1 Method of computation

The calculation falls into two parts: (a) the determination of the wave functions of the diffracted beams which emerge from a specimen when it is illuminated at specific angles by a parallel beam of electrons, and (b) the transformation of these functions into the image observed in a real electron microscope.

2.1.1. Diffraction

The formulation used is that of Cowley & Moodie (1957). Pictorially the crystal, of thickness H, is considered to be divided into slices and the potential within each slice is projected on to an internal plane. The effect on an incident electron beam is then described by the aggregate of the changes of phase produced successively by the projected potential, and propagation between the planes of projection.

Thus, if the potential in the nth slice, of thickness Δz, is φ_n (x,y,z), the projected potential is $\varphi_n(x,y) =$

$$\int_z^{z+\Delta z} \varphi_n (x,y,z) \mathrm{d}z,$$ and the corresponding change of

phase is $\exp(i\sigma\varphi_n)$, where $\sigma = \dfrac{\pi}{W\lambda} \cdot \dfrac{2}{1+(1-\beta^2)^{1/2}}$ and W

is the accelerating voltage, λ is the relativistic wavelength of the incident electrons with velocity v, and $\beta = v/c$.

Between planes, the electrons may be thought of as propagating in spherical waves, but for fast electrons these may be approximated by paraboloidal waves, so that the phase change due to propagation is given by

$\exp\left[\dfrac{ik(x^2+y^2)}{2\Delta z}\right]$. The principle of superposition allows

those phase changes, resulting from propagation from each part of the wavefront, to be added, so that, if ψ_n is the wave function for the nth slice,

$$\psi_{n+1} = \left\{\psi_n * \exp\left[\frac{ik(x^2+y^2)}{2\Delta z}\right]\right\} \exp\{i\sigma\varphi_{n+1}\} \qquad (1)$$

where $*$ represents convolution. In the impulse limit, as $\Delta z \to 0$, $n \to \infty$, $n\Delta z \to H$, this difference equation becomes the Schrödinger equation for forward scat-

tering. Limitation to forward scattering results from the approximation of spherical waves by paraboloidal waves. Thus this simple description is formally exact in the limit.

Propagation through the sequence of slices may be described recursively from equation (1), the resulting expression evaluated and the limits taken. This leads to a complete analytical solution (Cowley & Moodie, 1957), but in a form unsuitable for numerical computation. Further, no known transformations of this result are any more rapidly convergent (Cowley & Moodie, 1962; Moodie 1972a).

For the purposes of numerical estimation an iterative scheme based on equation (1) is therefore used. A major simplification is, however, possible. The potential $\varphi(x,y,z)$ is periodic, hence $\varphi_n(x,y)$, $\exp\{i\sigma\varphi_n\}$ and ψ_n are also periodic. Thus U_n, the Fourier transform of ψ_n is discrete, consisting of a set of delta functions, the orders of diffraction. This discrete set is, of course, very much easier to handle than the continuous function of equation (1). Accordingly, equation (1) is Fourier transformed to give a momentum representation,

$$U_{n+1} = U_n \exp\left[-i2\pi\zeta(h,k)\Delta z\right] * Q_{n+1} \qquad (2)$$

where $\zeta(h,k) = (u^2+v^2)\lambda/2$ is the excitation error for the beam (h,k), and Q_{n+1} is the Fourier transform of $\exp[i\sigma\varphi_{n+1}]$.

Repeated application of this relation generates the diffraction pattern as a function of thickness. The form is well suited to programming on a digital computer, and large numbers of beams, of the order of several hundreds, can be handled without excessive demands on fast store (Goodman & Moodie, 1972). In dynamical scattering, in general, non-zone or upper layer line reflexions couple in; i.e. in terms of microscopy, structure in the direction in which the beam is travelling modifies the image. It is this phenomenon which largely determines the choice of Δz; the greater the effect, the smaller the slice thickness permissible for a given accuracy (Goodman & Moodie, 1972; Lynch, 1971).

Crystal symmetry can be exploited by noting the symmetries of $\exp[i\sigma\varphi_n]$, thereby increasing the speed of the computation. The only remaining symmetries relate to reciprocity.

The details relating to the application of this technique to $W_4Nb_{26}O_{77}$ are given in Part II of this series (Lynch & O'Keefe, 1972).

2.1.2 Image in a real electron microscope

In an ideal electron microscope, a series of thin lenses would Fourier transform U_n to yield the magnified image $\psi\psi^*$. In a real electron microscope, however, the following perturbations must be incorporated.

(a) Objective aperture. The effects of an objective aperture can be estimated by multiplying the diffraction amplitude distribution by an appropriate aperture function. In practice, all that is required is to exclude all but an appropriate number of terms from the final

Fourier transformation.

(*b*) *Spherical aberration of the objective lens.* The effect of spherical aberration is to retard the phase of a plane wave passing through the lens at an angle α to the optical axis, by an amount $\frac{\pi}{2\lambda} C_s\alpha^4$ with respect to the axial ray at the Gaussian image plane. Here C_s is the spherical aberration coefficient. This phase change is incorporated in the diffraction amplitude distribution before the final Fourier transformation to give the image.

(*c*) *Chromatic aberration.* The thermal energy spread in a typical electron microscope is of the order of 0·5 eV. This range of voltage gives rise to a negligible variation in diffraction amplitude; in fact, to current experimental accuracies in microscopy, the direct effect of voltage spread on scattering can be neglected.

Chromatic aberration in the objective lens, however, results in different wavelengths being brought to focus on different planes, typically over a range of 20–60 nm. In many structures, image detail will change appreciably over such defects of focus, and a correction must be made by averaging the intensity distribution over the range.

(*d*) *Divergence of the incident beam.* The divergence of the electron beam incident upon a specimen in the electron microscope depends on the type of source and the settings of the condenser lenses, or the size of the condenser aperture. For imaging, the semi-angle, defined by the size of the condenser aperture, is usually about 10^{-3} rad. In order to take this divergence into account when computing in-focus images, it is necessary to determine the variation of intensities of the diffracted beams with angle of incidence up to the known divergence, and to sum the intensities in the image up to the same angle. For out-of-focus images, the rays passing through an image point come from adjacent parts of the object for deviated rays, and so point resolution is progressively lost with increasing departure from the Gaussian focus, and divergence.

Both effects must be considered, but the former is only important for thick crystals.

(*e*) *Astigmatism.* The facilities for correction astigmatism in modern electron microscopes are sufficiently precise to enable residual astigmatism to be reduced to levels which can be ignored.

(*f*) *Defect of focus.* For a defect of focus ε the wave function is evaluated at a distance ε from the exit surface of the crystal; *i.e.* the wave function is convoluted with $\exp\left[\frac{ik(x^2+y^2)}{2\varepsilon}\right]$. Again, for a periodic object, it is easier to evaluate the product of the amplitude of the diffraction pattern with $\exp[-i2\pi\zeta\varepsilon]$.

2.2 *Approximations*

While the methods of the previous section provide a means for computing images under a variety of conditions, they do not suggest any ready means of inter-

pretation. Direct interpretation in terms of charge density is, however, frequently possible for thin crystals. The basis for this follows from a consideration of the high voltage limit (HVL); *i.e.* the form which the scattering takes as the wavelength tends to zero. A rigorous discussion is possible (Cowley & Moodie, 1962; Moodie, 1972*b*) but for the present purposes the result may be obtained by taking formal limits in equation (1), giving

$$\psi_{HVL}=\lim_{\lambda\to0}\psi_{n+1}=\psi_n\exp\left[i(\lim_{\lambda\to0}\sigma)\varphi_{n+1}\right]$$

and

$$\lim_{\lambda\to0}\sigma=\left(\frac{2\pi m_0}{h^2}\right)\cdot\lim_{v\to c}\left(\frac{h}{m_0v}\right)=\left(\frac{2\pi m_0}{h^2}\right)\cdot\left(\frac{h}{m_0c}\right)$$

$$=\frac{2\pi m_0\lambda_c}{h^2}=\sigma_c,\qquad(3)$$

where v is the velocity and m_0 the rest mass of the incident electrons, and λ_c is the Compton wavelength. Thus,

$$\psi_{HVL}=\exp[i\sigma_c\varphi_p(x,y)]$$

and

$$U_{HVL}=\mathscr{F}\exp[i\sigma_c\varphi_p(x,y)]\qquad(4)$$

where $\mathscr{F}$ is the Fourier transform operator and φ_p is the projected potential $=\int_0^H\varphi(x,y,z)dz$.

The function $\exp[i\sigma_c\varphi_p]$ is more rapidly changing than φ_p, so that except for very thin crystals, extremely
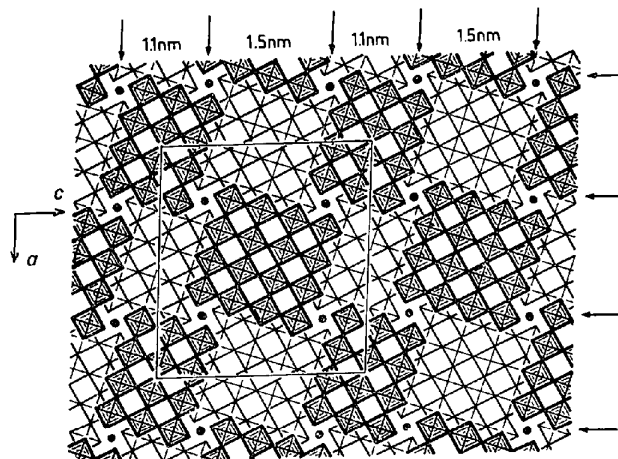

Fig. 1. Idealized model of the structure of $W_4Nb_{26}O_{77}$, viewed down [010]. Each square represents an octahedron, the lighter and darker squares being centred on parallel planes 0·19 nm apart. The octahedra form blocks of 4 × 3 and 4 × 4 by sharing corners, and these blocks are joined to one another by sharing octahedral edges along the crystallographic shear planes (arrowed). The circles represent tungsten atoms in tetrahedral coordination.

fine sampling intervals are required in the numerical estimation of the Fourier transform. In practice therefore, equation (4) is evaluated for a sufficiently thin slice of crystal, and the result for the required thickness obtained by the use of equation (1) with unit propagator (Lynch & O'Keefe, 1972). For the present purpose however, equation (4) is useful in interpretation, since under the conditions where ψ may be approximated by ψ_{HVL} an appeal may be made to the techniques of phase contrast microscopy. Zernike's (1942) classical solution cannot be used, since apart from the experimental difficulty of preparing and maintaining a quarter-wave plate, σ is some three orders of magnitude greater for electrons than photons, with the result that $\mathscr{F} \exp\{i\sigma\varphi_n\}$ cannot be approximated by $\delta(u,v) + i\sigma\mathscr{F}\varphi_p$.

Direct interpretation of defect of focus images in terms of charge density is, however, possible. Specifically, for infinite aperture,

$$I(x,y) = 1 - \frac{\varepsilon\lambda\sigma}{2\pi}\nabla^2\varphi_p = 1 - 2\varepsilon\lambda\sigma\varrho_p \qquad (5)$$

where I is the image contrast and ϱ_p the projected charge density. Details are given in Cowley & Moodie (1960) and in Moodie (1972b), but the result depends essentially on the equations for the defect of focus given in section 2.1.2. The diffraction amplitude is multiplied by $\exp[-i2\pi\zeta\varepsilon]$ for a defect of focus ε, or equivalently, by $\exp[-i\pi\lambda\varepsilon(u^2+v^2)]$. If ε is small in the sense that $\pi\lambda\varepsilon(u^2+v^2)\ll 1$, the exponential may be approximated by its first two terms. Since multiplication of a function by the square of its coordinates is equivalent to double differentiation of the Fourier transform of the function, the result follows on using Poisson's equation, $\nabla^2\varphi_p = 4\pi\varrho_p$. There is no direct analogue in light microscopy, since the second differential of the refractive index does not correspond to any easily visualizable physical quantity.

The relation (5) applies equally to periodic and nonperiodic objects, so that the charge distribution of a lattice, and of a defect in it, can be imaged under the same conditions and in the same field. Further, it has been verified experimentally (Moodie, 1972b) that appropriate defocusing generates the sign, as well as the magnitude of the charge density.

The approximation (5) is applicable when the Ewald sphere is effectively planar. This may be tested directly by comparing the images obtained at different accelerating voltages. Alternatively, the images obtained at small intervals of focus near zero defect of focus may be compared to determine whether the only variations are those of contrast.

The intensity distribution in the high voltage limit, and for limited aperture is, to the first order in ε and σ,

$$_lI_\varepsilon = (\bar{C}^2 + \bar{S}^2) - 2\varepsilon\lambda\sigma(\bar{C}\cdot\overline{C\varrho_p} + \bar{S}\cdot\overline{S\varrho_p}), \qquad (6)$$

where $C = \cos(\sigma\varphi_p)$, $S = \sin(\sigma\varphi_p)$, and typically, $\bar{C} =$

$C * \mathscr{S}$ and $\overline{C\varrho_p} * \mathscr{S}$, where $\mathscr{S}$ is the shape transform of the aperture. Comparison with equation (5) shows that contrast reverses through the Gaussian focus only when the aperture is effectively infinite, since the first term of equation (6) gives finite contrast at zero defect of focus. This is the conventional restricted aperture term, and tends to have maxima in the same regions as the charge density, so that in some cases, the perturbing effect of this term will not be too great. It introduces an asymmetry into images on going through focus, but the perturbation reinforces the contrast in under-focused images to give a better representation of the charge distribution. Furthermore, in real electron microscopes operated with large objective apertures spherical aberration will introduce additional serious perturbations.

In practice, it is necessary to record a through-focus series. An image may be interpreted in terms of projected charge density at a certain level of resolution if, at the same level of resolution, the contrast reverses through the Gaussian focus, and the profile of the lattice fringes changes only in amplitude in the vicinity of zero defect of focus. A further check can be made by repeating the observations at another wavelength. If these conditions cannot be satisfied, a complete calculation must be made, possibly using an approximate interpretation as a guide. Calculations of this type, which are presented here, make no excessive demands on current digital computers, even for large unit cells. It has been found that attempts at semiquantitative argument, though sometimes plausible, are liable to serious error.

3. The crystal structure of $W_4Nb_{26}O_{77}$

$W_4Nb_{26}O_{77}$ is monoclinic, space group $C2$, and its unit cell has the dimensions $a = 2\cdot974$ nm, $b = 0\cdot3824$ nm, $c = 2\cdot597$ nm, $\beta = 1\cdot611$ rad. Its crystal structure (Andersson, Mumme & Wadsley, 1966) shown in an idealized way in Fig. 1, contains discrete blocks of corner-shared MeO_6 octahedra ($Me = $ metal ion). The blocks themselves are joined together by sharing octahedral edges, and tetrahedral sites at the corners of the blocks are occupied by additional metal atoms. The regions where the blocks are joined are referred to as crystallographic shear (CS) planes (Wadsley, 1955), and form a grid parallel to $\langle 010 \rangle$, marked by arrows in Fig. 1.

$W_4Nb_{26}O_{77}$ may be described as an ordered intergrowth of two simpler structures, $WNb_{12}O_{33}$ (Roth & Wadsley, 1964a) and $W_3Nb_{14}O_{44}$ (Roth & Wadsley, 1964b), in which the blocks are 4×3 and 4×4 octahedra in cross-section respectively. $W_4Nb_{26}O_{77}$ contains alternate slabs of these two structures, running parallel to a, as shown in Fig. 1. For this reason, the CS planes in this direction are spaced alternately $1\cdot1$ nm (across a 4×3 block) and $1\cdot5$ nm (across a 4×4 block) apart. Our previous electron microscope study of this compound (Allpress, Sanders & Wadsley, 1969) indicated that these alternate spacings could be revealed in

lattice images, and that irregularities in the sequence of slabs were quite common. Both these features can be seen, for example, in Fig. 3.

4. Experimental

A microcrystalline sample of $W_4Nb_{26}O_{77}$ was kindly provided by the late Dr A. D. Wadsley. The sample was ground in an agate mortar and slurried with methyl chloroform. Fracture fragments were scooped from this slurry on to a carbon-coated specimen grid, and examined at 100kV in a JEM 100B electron microscope fitted with a double tilting specimen holder.

When a suitable thin fragment of material was found, it was oriented so that its *b* axis lay parallel to the incident electron beam [Fig. 2(*a*)] and then tilted about the c^* axis by about 0·1 rad, until the diffraction pattern contained a symmetric, systematic set of 00*l* reflexions, accompanied by ± 207 and weak ± 205 spots [Fig. 2(*b*)]. After inserting an objective aperture of 70 μm diameter, which restricted the number of contributing diffracted beams to $\pm 00l$ with $l \leq 5$, a series of eleven images was recorded at a magnification of about 400 000 ×, at 136 nm (nominal) increments of focus, equally spaced on either side of the Gaussian image plane. The position of the latter was estimated from the appearance of Fresnel fringes at the edge of the fragment. A diffraction pattern was recorded on the last plate of each set of twelve, without changing the illuminating conditions. The divergence of the incident beam of electrons, determined from these diffraction patterns, was 6×10^{-4} rad (semi-angle).

In order to improve the signal-to-noise ratio in the final photographic prints, a cylindrical lens was mounted immediately below the lens of the enlarger, with its axis normal to the direction of the fringes in the lattice images. This technique of image enhancement (Dowell, Farrant & McLean, 1968) is valid for this case of a set of parallel fringes, and makes a marked improvement to the clarity of the images.

The computations were carried out on IBM 7044 and CDC 3200/3600 machines, using programs written in Fortran. Computed images, three unit cells in width, were presented either as intensity profiles or as half tone images (Head, 1967) on a line printer. The latter were found to be particularly useful for rapid inspection and qualitative comparison with experimental images.

For thicknesses up to 60 nm, a full two-dimensional computation was made, using 435 diffracted beams. A slice thickness of 1 nm perpendicular to the incident beam was used, and was made up by convolution of ten 0·1 nm phase gratings (Lynch & O'Keefe, 1972). A simpler systematics calculation, using only 29 00*l* diffracted beams ($-14 < l < +14$), was employed for thicknesses up to 100 nm. In both cases, the atomic positions determined by Andersson, Mumme & Wadsley (1966) for $W_4Nb_{26}O_{77}$, and scattering factors for neutral atoms, were used.

5. Results

5.1 *Experimental observations*

5.1.1. '*Best contrast*' images

Fig. 3(*a*) shows a lattice image from a typical thin fragment of $W_4Nb_{26}O_{77}$, in which the objective lens was focused for best image contrast. Over most of the field, there is a regular arrangement of alternating wide and narrow white fringes, lying perpendicular to c. A microdensitometer record of the fringe profile in the area marked *X–X* is shown in Fig. 3(*b*). The valleys in Fig. 3(*b*) correspond to black lines in Fig. 3(*a*), and they are spaced alternately about 1·1 and 1·5 nm apart. At the places marked *B* and *N* in Fig. 3(*a*), the regular sequence is interrupted by the presence of additional broad or narrow white fringes respectively. These are Wadsley defects, involving the disordered intergrowth of the parent phases $W_3Nb_{14}O_{44}$ and $WNb_{12}O_{33}$, and models of them have been proposed previously (Allpress, Sanders & Wadsley, 1969). together with that of a more complex displacement defect similar to the one which is circled in Fig. 3(*a*).

From observations of the Fresnel fringes at the edges of fragments, it was observed that the best contrast in the lattice images was obtained when the objective lens was slightly underfocused (about -100 nm) with respect to the Gaussian image plane.

5.1.2 *Through-focus series*

A number of series of images from different crystals were found to contain similar fringe contrast, which changed systematically with defect of focus. The best set was selected and the clearest parts enlarged to produce strips of image, containing a Wadsley defect (Fig. 4) for comparison with computations. In this series, the image labelled $+30$ was found to be closest to the Gaussian image plane, following an examination of the Fresnel fringes at the edge of the fragment. The 'best contrast' image is obviously that marked -70, which is slightly underfocus with respect to the Gaussian image plane. This image contains a sequence of wide and narrow white bands similar to those in Fig. 3(*a*), and a Wadsley defect, consisting of two adjacent wide bands, occurs in the vicinity of the arrow. The images in Fig. 4 were aligned with respect to one another by using this defect as a reference, and assuming that the line about which the contrast on either side of the defect is symmetrical (arrowed) remains in a constant position. This criterion was difficult to apply at large defects of focus (*e.g.* in the image labelled $+430$), and the computed images (see below) were then used as a guide.

5.1.3 *Electron diffraction patterns*

The diffraction patterns which were recorded at the end of each through-focus series contained useful information, particularly if the area of the fragment selected for diffraction was as small as possible and of
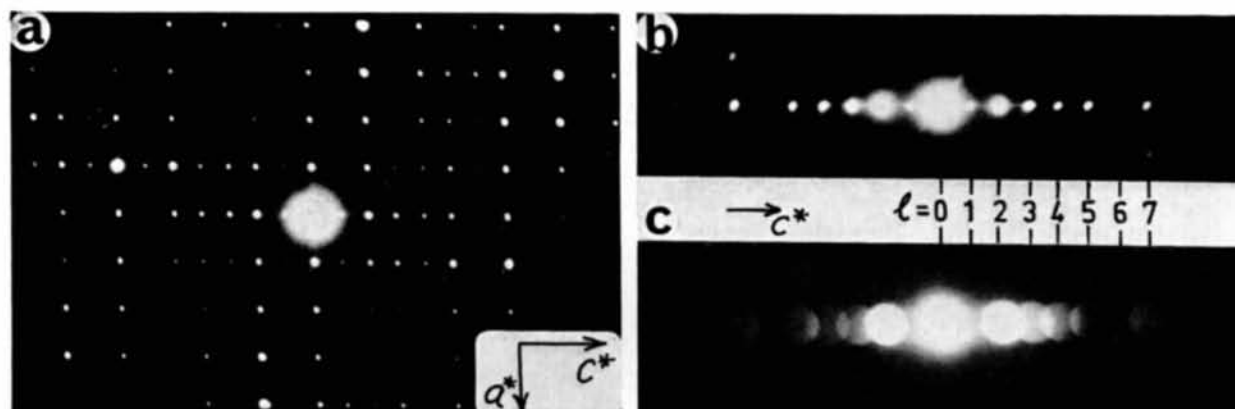
Fig. 2. Electron diffraction patterns from thin fragments of $W_4Nb_{26}O_{77}$. (a) $h0l$ reciprocal lattice section, obtained with the electron beam incident parallel to [010]. (b) $00l$ systematics orientation, obtained by tilting away from the orientation in (a) by ca. 0·2 rad about $\mathbf{c}^*$. (c) as for (b), but with focused illumination. Each spot now appears as a disc, from which divergence can be calculated, and intensity estimated.
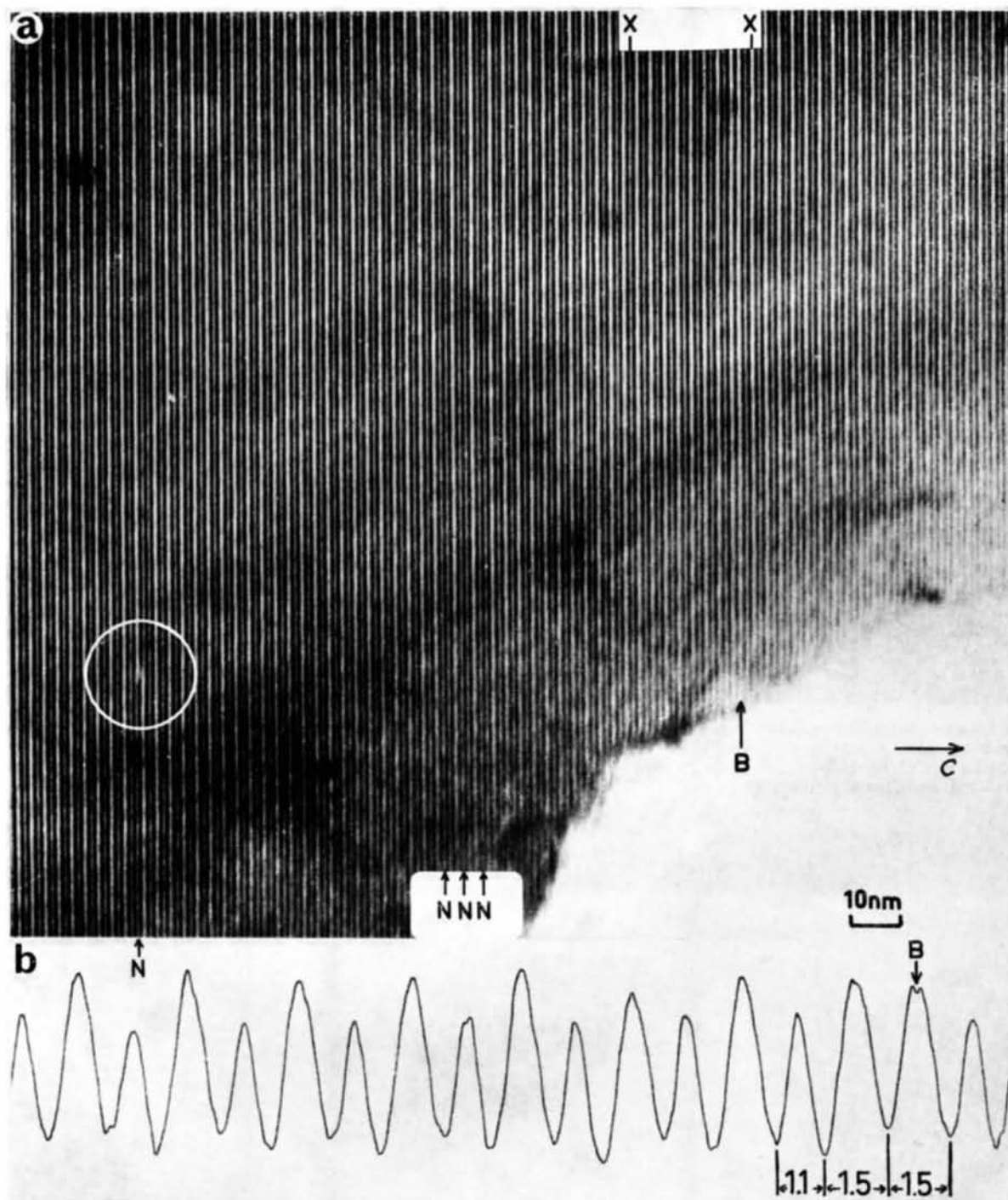
Fig. 3. (a) 00l lattice image from a thin fragment of $W_4Nb_{26}O_{77}$ showing a series of wide and narrow dark fringes, which alternate regularly except at B and N, which are Wadsley defects. A more complex displacement defect is circled. (b) Microdensitometer trace along the line X–X in (a). The valleys, which correspond to black lines in (a) are alternately 1·1 and 1·5 nm apart, except at the Wadsley defect B, where two 1·5 nm spacings occur together.
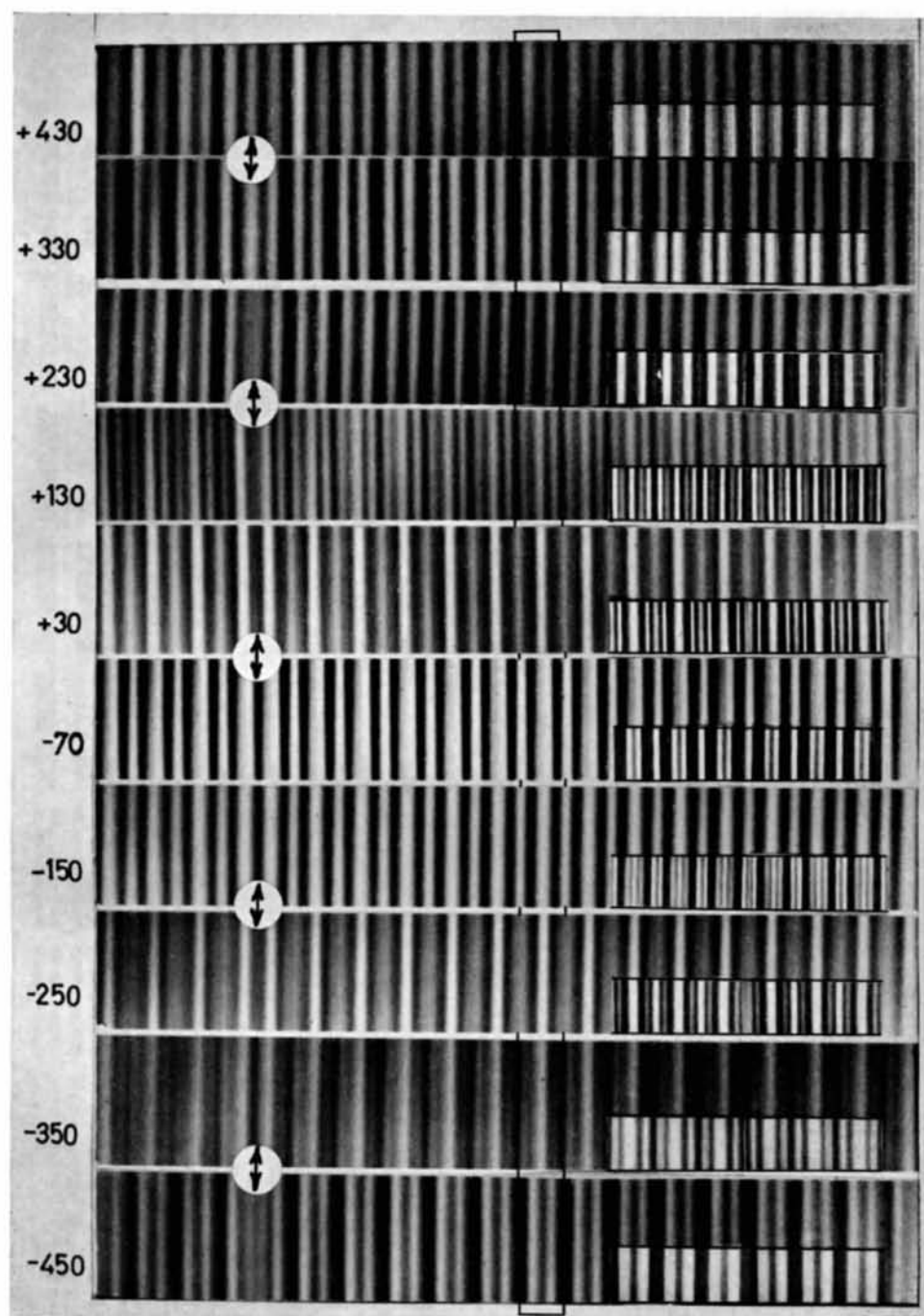
Fig. 4. Through-focus series of $00l$ ($|l| \leq 5$) lattice images from a thin fragment of $W_4Nb_{26}O_{77}$, containing a Wadsley defect (arrowed). The increments of focus were nominally 136 nm, and the Gaussian image plane lay between the images labelled +30 and −70. The unit cell is marked. The insets are images covering 6 unit cells, computed for a crystal 30 nm thick, and for the defects of focus (in nm) shown on the left of the figure. The effects of divergence and spherical aberration have been included.
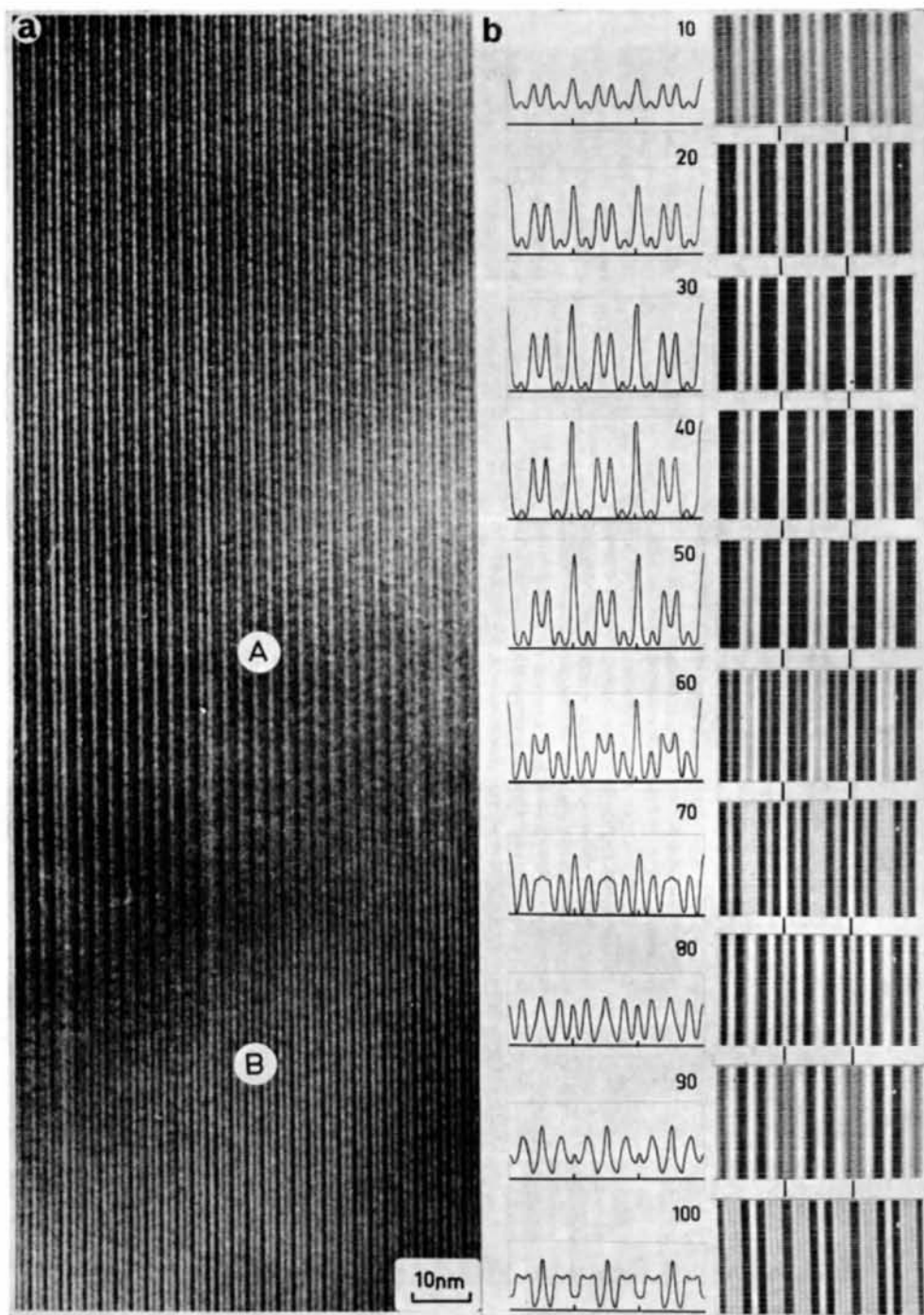
Fig. 6. (a) 00l lattice image from a crystal of $W_4Nb_{26}O_{77}$, whose thickness increases from top (thin) to bottom. Over the range of thickness A–B, there is a reversal of contrast. (b) Computed profiles and images of three unit cells of $W_4Nb_{26}O_{77}$, 30 nm thick, at −100 nm defect of focus, for thicknesses between 10 and 100 nm, as marked. The contrast remains relatively constant for thicknesses up to about 50 nm, but reverses over the next 50 nm. No detailed correspondence between (a) and (b) is intended.
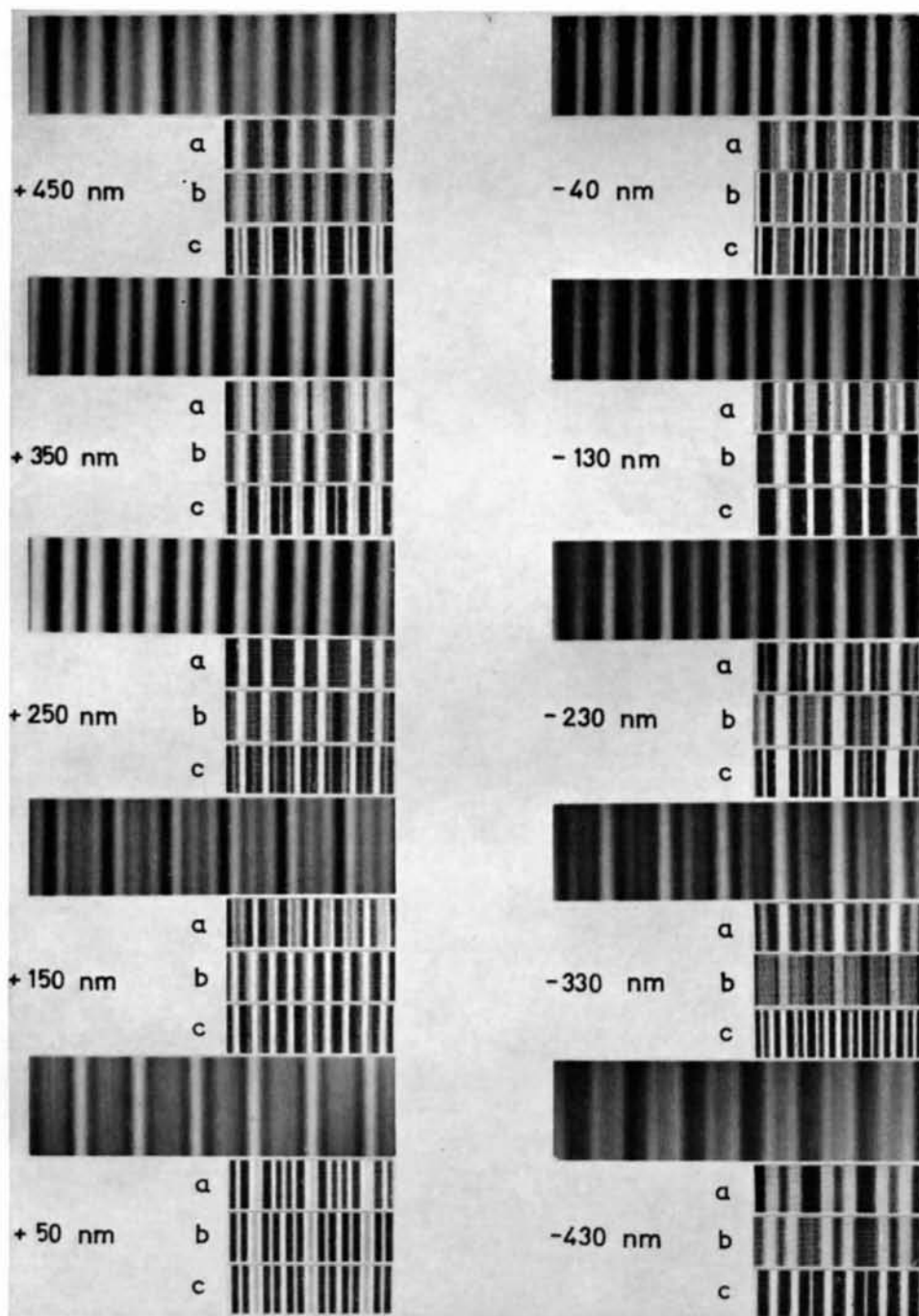
Fig. 7. Comparison of an observed through-focus series (larger images) and computed images (smaller), showing the effect of various instrumental factors. The numbers refer to the defects of focus for which the images were computed. (a) Corrected for divergence and spherical aberration. (b) Corrected for divergence only. (c) 'Ideal' image, with no corrections.

reasonably uniform thickness. Fig. 2(c) shows an example. Because the illumination conditions required for imaging were retained, the spots in the pattern appear as discs, from which the divergence of the incident beam is obtained. The intensities of the reflexions can be estimated qualitatively and compared with those calculated for a variety of crystal thicknesses.

5.2 Comparison of computed and experimental results

5.2.1 Diffraction intensities

Fig. 5 shows the phases and intensities of the first five 00l diffracted beams as a function of thickness. They were calculated using the systematics approximation, but a two-dimensional computation up to 60 nm gave substantially the same results. Below about 50 nm, there is little change in the relative phases and intensities, but at greater thicknesses, considerable variation appears, and the intensities exhibit extinction effects (Pendellösung). An inspection of Fig. 2(c) indicates that the observed intensities of the 00l reflexions are in qualitative agreement with the data in Fig. 5(b), for thicknesses between about 30 and 50 nm. In particular the 001 reflexion is very weak, and 002 is very strong.

5.2.2 Image contrast

In the first instance, a series of images were computed for thicknesses up to 100 nm, in increments of 10 nm, and for defects of focus up to ± 450 nm, using increments of 10 nm. The systematics approximation was employed initially, and the effects of instrument aberrations were ignored.
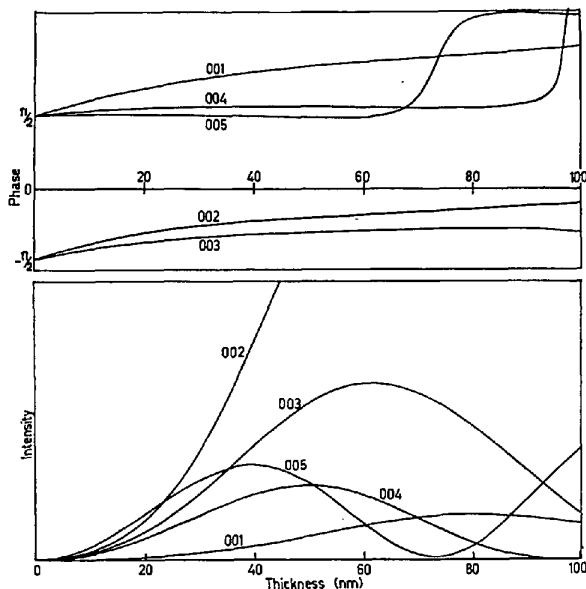

Fig. 5. Computed phases (a) and intensities (b) for 00l ($|l| \leq 5$) beams diffracted from $W_4Nb_{26}O_{77}$, as a function of thickness.

(a) Thickness (H)

The images used for comparison with computations were taken from micrographs of thin wedge-shaped fragments. It was established that these parts of similar crystals were about 30 nm thick, by measuring the projected width of a Wadsley defect when the crystal was tilted through a known angle (0·4–0·5 rad) about the a axis. Observation indicated that the appearance of the fringes was not sensitive to thickness near these edges, but did change within obviously thicker parts of the crystal. This effect is seen in Fig. 6(a), which shows the image of a fragment whose thickness increases from top to bottom. The contrast was constant from the edge of the crystal (not shown) down to the region A, but reverses over the region A–B. Computed images [Fig. 6(b)] show increasing contrast, but no change of character for thicknesses up about 50 nm; important changes occur at greater thicknesses, such that at 100 nm, the contrast is a reversal of that at 40–50 nm. While the experimental and computed results in Fig. 6 show the same trend with thickness we do not expect any quantitative correlation, because we have no independent measure of the thickness of the crystal, and we have used the approximate systematics calculation without corrections for important aberrations. Nevertheless, it is clear that for thicknesses between 20 and 50 nm, image contrast remains relatively constant. This result is not unexpected, since the computed diffraction data (Fig. 5) also showed little relative change over this range.

(b) Defect of focus (ε)

We adopt the convention that the electrons are propagated in a positive direction from the gun, through the crystal, and on to the plate; hence overfocus is a positive defect, and underfocus is negative.

The contrast of the fringes changes detectably for $\delta\varepsilon > 50$ nm, and there are marked changes between successive micrographs in Fig. 4, for which the nominal increment is 136 nm. The number of fringes per unit cell, and their width and intensity, all vary. For example, the appearance of the fringes at $+330$ and -450 is almost identical, and both are a reversal of the 'best contrast' image at -70.

The insets to Fig. 4 are computed images for a crystal 30 nm thick; a full two-dimensional 435 beam calculation was employed, and the effects of divergence of the incident beam and spherical aberration have been taken into account. The numbers on the left represent the defects of focus, ε, for which these images were computed. These images were the best visual fit to the experimental set, and were selected from a series computed at intervals of $\delta\varepsilon = 10$ nm, with the criterion that the intervals of focus should be as nearly constant as possible. The agreement between experimental and computed contrast is quite good, and extends to fine detail. The range of contrast is a little different, but no attempt has been made to adjust precisely the grey scale for the computed images.

(c) Divergence

The effect of variation of angle of incidence on the intensity of the diffracted beams which pass through the objective aperture was computed for an angle corresponding to the beam divergence. The mean variation in intensity for $H = 30$ nm was 7%, and the greatest variation was 15% for the 005 reflexion. It was considered that this variation would not alter the fringe contrast perceptibly, and that the main consequence of divergence would be the transposition as discussed in section 2.1.2 (d). The final images were obtained by adding intensities, translated by $^1/_{40}$ of a unit cell, for each 95 nm in the defect of focus, so that at the extremes of defect of focus, the summation was over eleven steps.

The effect of this transposition caused by divergence can be seen by comparing the computed images in Fig. 7, where those labelled (b) are corrected for divergence, and (c) has no correction. Near the Gaussian focus, the divergence has no appreciable effect. However, fine detail begins to be lost when $\delta\varepsilon \approx \pm 200$ nm, and the fringes become progressively more diffused with increasing defect of focus, so that at the extremes shown in Figs. 4 and 7, only two fringes per unit cell can be resolved.

(d) Spherical aberration

The manufacturer's information is that the spherical aberration coefficient C_s for the particular objective lens used lies between 3 and 5 mm, the range of values being due to the uncertainty in position introduced by the tilt of the specimen. We used $C_s = 5$ mm. This produces a negligible phase change for diffracted beams with $l \leq 4$. However, the fifth order beam, which has appreciable intensity [Fig. 5(b)], is affected and the consequences of including this correction can be seen by comparing the computed images (a: corrected, and b: uncorrected) in Fig. 7. It improves the fit to the experimental images, particularly in the neighbourhood of the Gaussian focus.

(e) Chromatic aberration

The effect of depth of focus produced by thermal spread of the incident electrons is slight (Lynch & O'Keefe, 1972). Only very fine detail, near the limit of resolution, is modified.

(f) Inelastic processes

For the thin crystals considered here it was unnecessary to include any absorption factors to obtain agreement between computed and experimental images.

6. Discussion

We have been able to reproduce the contrast in experimental through-focus series of 00l lattice images from thin crystals of $W_4Nb_{26}O_{77}$, using a 435-beam two-dimensional calculation with corrections for divergence and spherical aberration. A comparison of

the results of this, with other simpler but less reliable computations is given by Lynch & O'Keefe (1972). As can be seen from Fig. 7, the neglect of corrections for instrumental effects leads to a lack of correspondence in detail.

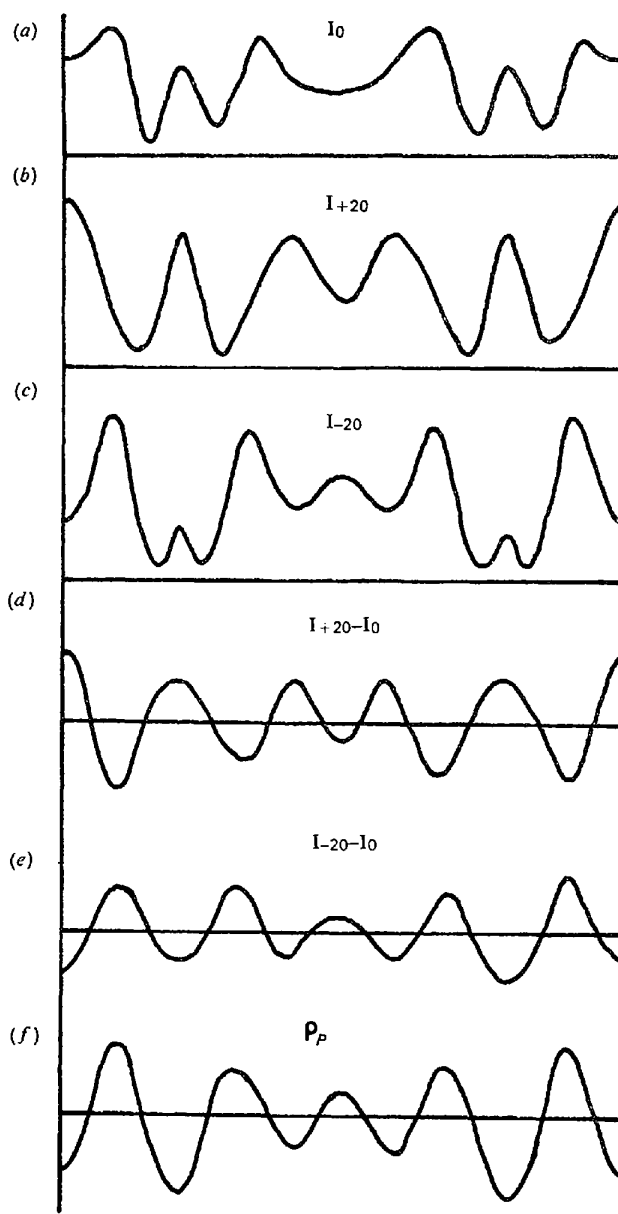It is obvious from an inspection of Fig. 4 that the criteria which were stated in section 2·2, which must

Fig. 8. (a), (b), (c) Computed intensity profiles I_ε across one unit cell of $W_4Nb_{26}O_{77}$, 30 nm thick, for 00l beams with $|l| \leq 5$, using a 435-beam calculation. The defects of focus, ε, are 0 (a), $+20$ nm (b), and -20 nm (c). (d), (e) Difference intensity profiles $I_{+20}-I_0$ (d), and $I_{20}-I_0$ (e), showing the reversal of the charge density component of the contrast. (f) Projected charge density, ϱ_p, computed for 00l beams with $|l| \leq 5$.

be met before an intuitive interpretation of contrast in terms of charge density is justified, are not satisfied in our experiment. The major reason for this is that we have restricted the number of contributing beams to 11 by inserting an objective aperture, and eliminated a number of intense beams which arise particularly from the strong ReO_3-type subcell (Fig. 1). The effect of this restriction can be seen by examining computed images near the Gaussian focus. Fig. 8(a–c) shows profiles of the contrast over one unit cell, for $\varepsilon = 0$, $+20$, and -20 nm respectively. It is clear from equation (6) (section 2·2) that at $\varepsilon = 0$, the intensity distribution, $I_0 = (\bar{C}^2\varepsilon + \bar{S}^2)$; i.e. at the Gaussian focus, the contrast is due entirely to aperture restriction. By substracting the intensity due to this term [Fig. 8(a)] from that at a near-focus position, I_ε, [Fig. 8(b, c)], the contrast due to the second term in equation (6) can be obtained. These difference profiles, $I_{+20} - I_0$ and $I_{-20} - I_0$, shown in Fig. 8(d, e) respectively, represent the charge density component of the contrast, and exhibit the reversal expected from equation (5). The underfocus difference profile (e) is a good representation of the projected charge distribution, ϱ_p, for $00l$ beams with $|l| \leq 5$, which is shown in Fig. 8(f). We believe that this procedure may be quite useful, but further consideration of the second term in equation (6), and the effect of spherical aberration is required before the extent of its applicability can be established.

Ideally, it is obviously desirable to work without an aperture, but two experimental factors intervene: (a) all those beams hkl for which d_{hkl} is less than the resolution of the instrument will contribute only to background and reduce the contrast, (b) the phases of additional beams will be increasingly modified by the spherical aberration of the objective lens. While this effect can be computed, it will certainly hinder an intuitive interpretation. In our case, the influence of spherical aberration, is only significant for the ± 005 beams, and therefore has little influence on the lattice images.

The computations have shown that for slightly underfocused images ($\varepsilon = -40$ and -130 nm in Fig. 4) lines of dark contrast appear in positions which correspond directly with those of the crystallographic shear planes in the structure (Fig. 1). These planes are spaced alternately 1·102 and 1·495 nm apart in the structure, and 0·551 nm from the edge of the unit cell. The corresponding positions of the centres of black bands in computed images are 1·10, 1·50 and 0·55 nm at $\varepsilon = -40$ nm, and 1·07, 1·53 and 0·54 nm at $\varepsilon = -130$ nm. This confirms the previous interpretation of experimental images (Allpress, Sanders & Wadsley, 1969), which was based on the assumption that thin fragments of this and other related materials were behaving as thin phase gratings, and that the contrast at small negative defects of focus reflected the charge density in the structure (Cowley & Moodie, 1960).

While the calculations have been restricted to a single structure, it seems reasonable to expect a similar result for others of the large number of related materials which contain blocks of the ReO_3-type structure joined by crystallographic shear planes (Wadsley & Andersson, 1970). Observations which have been made on many of these compounds (Allpress, Sanders & Wadsley, 1969; Allpress & Wadsley, 1969; Allpress, 1969a) are consistent with this conclusion.

More recent applications of lattice imaging to these materials have involved the use of a two-dimensional set of $h0l$ reflexions rather than a single line of systematics (Allpress, 1969b, 1970; Allpress & Roth, 1970; Iijima, 1971; Allpress & Sanders, 1972; Cowley & Iijima, 1972). In this orientation, the electron beam is incident parallel to the short b axis of the structures (i.e. perpendicular to the plane of the projection in Fig. 1), and the images contain a wealth of detail which, under suitable conditions of defocus, can be correlated directly with structural features. The high resolution images obtained by Iijima (1971) are particularly impressive in this respect, and contain sufficient information to enable unequivocal models for ordered structures and defects to be proposed. From a theoretical viewpoint, there is no difficulty in principle involved in extending our computation procedures so as to handle two-dimensional images, and some preliminary calculations on the high-temperature form of Nb_2O_5 (Chidzey, 1970) have yielded encouraging results. Experimentally, it is observed that very thin crystals, of the order of 5–10 nm in thickness, are required in order to obtain useful images.

It must be emphasized that the images with which we are concerned here, being formed from many more than two (in fact, eleven in the systematics case, and upwards of fifty in the two-dimensional case) beams passing through the objective aperture, bear little resemblance to the fringes from a two-beam situation. In the latter case, it has been shown that it is quite misleading to relate fringe positions directly with structure (Hashimoto, Mannami & Naiki, 1961), or to relate terminating fringes directly with dislocations (Cockayne, Parsons & Hoelke, 1971). The difference arises primarily from the difference in the size of the unit cells. The large unit cells allow many beams to be included through an aperture of a size selected to avoid modifications by spherical aberration, and extinction distances are sufficiently large that crystals up to 10 nm or more in thickness are still effectively 'thin'.

References

ALLPRESS, J. G. (1969a). *J. Solid State Chem.* **1**, 66.
ALLPRESS, J. G. (1969b). *Mater. Res. Bull.* **4**, 707.
ALLPRESS, J. G. (1970). *J. Solid State Chem.* **2**, 78.
ALLPRESS, J. G. & ROTH, R. S. (1970). *J. Solid State Chem.* **2**, 366.

ALLPRESS, J. G. & SANDERS, J. V. (1972). In *Electron Microscopy and structure of Materials*. Edited by G. THOMAS, p. 134. Berkeley, California: Univ. of California Press. (To be published).

ALLPRESS, J. G., SANDERS, J. V. & WADSLEY, A. D. (1969). *Acta Cryst.* B25, 1156.

ALLPRESS, J. G. & WADSLEY, A. D. (1969). *J. Solid State Chem.* 1, 28.

ANDERSSON, S., MUMME, W. G. & WADSLEY, A. D. (1966). *Acta Cryst.* 21, 802.

CHIDZEY, E. A. (1970). M. Sc. Thesis, University of Melbourne.

COCKAYNE, D. J. H., PARSONS, J. R. & HOELKE, C. W. (1971). *Phil. Mag.* 24, 139.

COWLEY, J. M. (1967). In *Progress in Materials Science*. vol. 13, No. 6, p. 267, Edited by B. CHALMERS and W. HUME-ROTHERY. Oxford: Pergamon Press.

COWLEY, J. M. & IIJIMA, S. (1972). *Z. Naturforsch.* 27a, 445.

COWLEY, J. M. & MOODIE, A. F. (1957). *Acta Cryst.* 10, 609.

COWLEY, J. M. & MOODIE, A. F. (1960). *Proc. Phys. Soc.* 76, 378.

COWLEY, J. M. & MOODIE, A. F. (1962). *J. Phys. Soc. Japan*, 17, Suppl. BII, p. 86.

DOWELL, W. C. T. (1963). *Optik*, 20, 535

DOWELL, W. C. T., FARRANT,. J. L. & McLEAN, J. D. 1968. In *Proceedings of the Fourth European Regional Conference on Electron Microscopy, Rome*, p. 583.

GOODMAN, P. & MOODIE, A. F. (1972). Submitted to *Acta Cryst.*

HASHIMOTO, H., MANNAMI, M. & NAIKI, T. (1961). *Phil. Trans.* A253, 459.

HEAD, A. K. (1967). *Aust. J. Phys.* 20, 557.

IIJIMA, S. (1971). *J. Appl. Phys.* 42, 5891.

LYNCH, D. F. (1971). *Acta Cryst.* A27, 399.

LYNCH, D. F. & O'KEEFE, M. A. (1972). *Acta Cryst.* A28, 536.

MOODIE, A. F. (1972a). *Z. Naturforsch.* 27a, 437.

MOODIE, A. F. (1972b). Submitted to *Phil. Mag.*

MIYAKE, S., FUJIWARA, K., TOKONAMI, M. & FUJIMOTO, F. (1964). *Jap. J. Appl. Phys.* 3, 276.

ROTH, R. S. WADSLEY, A. D. (1964a). *Acta Cryst.* 19, 32.

ROTH, R. S. & WADSLEY, A. D. (1964b) *Acta Cryst.* 19, 38.

WADSLEY, A. D. (1955.) *Rev. Pure Appl. Chem.* 5, 165.

WADSLEY, A. D. & ANDERSSON, S. (1970). In *Perspectives in Structural Chemistry*, Vol. 3, p.1. Edited by J. D. DUNITZ & J. A. IBERS, New York: Wiley.

YADA, K. & HIBI, T. (1969). *J. Electron Microsc.* 18, 266.

ZERNIKE, F. (1942). *Physica*, 9, 686.

n-Beam Lattice Images.
II. Methods of Calculation

BY D. F. LYNCH

Division of Chemical Physics, CSIRO, P. O. Box 160, Clayton, Victoria, Australia, 3168

AND M. A. O'KEEFE

Division of Tribophysics, CSIRO, University of Melbourne, Victoria, Australia, 3052

The calculation of amplitudes and phases of beams of electrons diffracted from thin ($\leq$ 100 nm) crystals of $W_4Nb_{26}O_{77}$ is described. These diffraction data are used to compute 11-beam 00*l* electron microscope lattice images and the effects of instrument aberrations are considered. Several approximations are compared with a more exact 435-beam, two-dimensional computation, and with experimental diffraction data and lattice images. Finally, the projected charge density approximation to image contrast is evaluated.

1. Introduction

In the first paper in this series (Allpress, Hewat, Moodie & Sanders, 1972) (referred to as I hereafter), an account of the theory of electron scattering and imaging is given. The agreement obtained between experimental and calculated images is shown to be quite good when applied to 11-beam, 00*l* images from the complex oxide $W_4Nb_{26}O_{77}$. In this paper, calculations which produce these results are described and ways given to incorporate instrumental effects in the calculation. The effects include:

  (i) Spherical aberration

  (ii) Chromatic aberration

  (iii) Beam divergence.

Methods of calculation of electron scattering problems have been described elsewhere (Cowley & Moodie, 1957; Goodman & Moodie, 1972). These use both multislice and phase-grating methods to calculate